nature synthesis



Article

https://doi.org/10.1038/s44160-024-00731-1

Cyclopalladation of a covalent organic framework for near-infrared-light-driven photocatalytic hydrogen peroxide production

Received: 22 August 2024

Accepted: 18 December 2024

Published online: 10 February 2025

Check for updates

Andrés Rodríguez-Camargo ® ^{1,2}, Maxwell W. Terban¹, Martina Paetsch ® ^{1,2}, Elio A. Rico³, Daniel Graf ® ⁴, Radhika Hirpara², Viola Duppel ® ¹, Igor Moudrakovski¹, Martin Etter ® ⁵, Néstor Guijarro ® ³, Christian Ochsenfeld ^{1,4}, Robert E. Dinnebier ¹, Liang Yao ® ⁶ ≈ & Bettina V. Lotsch ® ^{1,2,4} ≈

Covalent organic frameworks (COFs) have been developed as photosensitizers for photocatalytic energy conversion over the past decade; however, COF photocatalysts have yet to demonstrate the ability to harvest near-infrared light (above 760 nm, approximately 53% of the solar spectrum) for fuel or chemical conversion. In this work we introduce a post-synthetic functionalization strategy for COFs by incorporating a palladacycle directly into the COF backbone, extending the light absorption of an azobenzene-based COF into the near-infrared region. This approach enables homogeneous, atomically distributed palladium functionalization with a high loading of 12 wt% and without noticeable formation of palladium nanoparticles. The cyclopalladated COF, TpAzo-CPd, was used as a catalyst for photocatalytic hydrogen peroxide production under 810 nm illumination. This study demonstrates the use of COFs for near-infrared photocatalysis and opens the door to palladium-single-site COF catalysts for a wide range of chemical transformations.

Since the first demonstration in 2005 (ref. 1), covalent organic frameworks (COFs) have emerged as a powerful platform for creating functional porous materials by covalently linking a variety of building blocks. The customizable molecular structures and functionalities of COFs offer promising routes to applications in diverse fields, such as gas storage and separation^{2,3}, sensing⁴, water harvesting^{5,6} and drug delivery^{7,8}. In 2014, our group demonstrated⁹ the use of COFs as light-harvesting materials for photocatalytic solar energy conversion, enabling the storage of solar energy in the form of hydrogen

fuel. Covalent organic frameworks have since rapidly evolved as photocatalysts for solar energy conversion and have been successfully employed in various reactions, including CO_2 reduction¹⁰, organic pollutant degradation¹¹ and the oxidative hydroxylation of arylboronic acids to produce phenols¹². However, photocatalytic reactions driven by COFs have so far been restricted to using visible light (<760 nm). There is a burgeoning interest in exploiting near-infrared light (NIR > 760 nm) for photocatalytic applications, particularly as NIR light comprises approximately 53% of the solar spectrum¹³.

¹Max Planck Institute for Solid State Research, Stuttgart, Germany. ²Department of Chemistry, University of Stuttgart, Stuttgart, Germany. ³Institute of Electrochemistry, University of Alicante, Alicante, Spain. ⁴Department of Chemistry, University of Munich (LMU), Munich, Germany. ⁵Deutsches Elektronen-Synchrotron (DESY), Hamburg, Germany. ⁵State Key Laboratory of Luminescent Materials and Devices, Institute of Polymer Optoelectronic Materials and Devices, Guangdong Basic Research Center of Excellence for Energy and Information Polymer Materials, South China University of Technology, Guangzhou, P. R. China. ⊠e-mail: liangyao@scut.edu.cn; b.lotsch@fkf.mpg.de

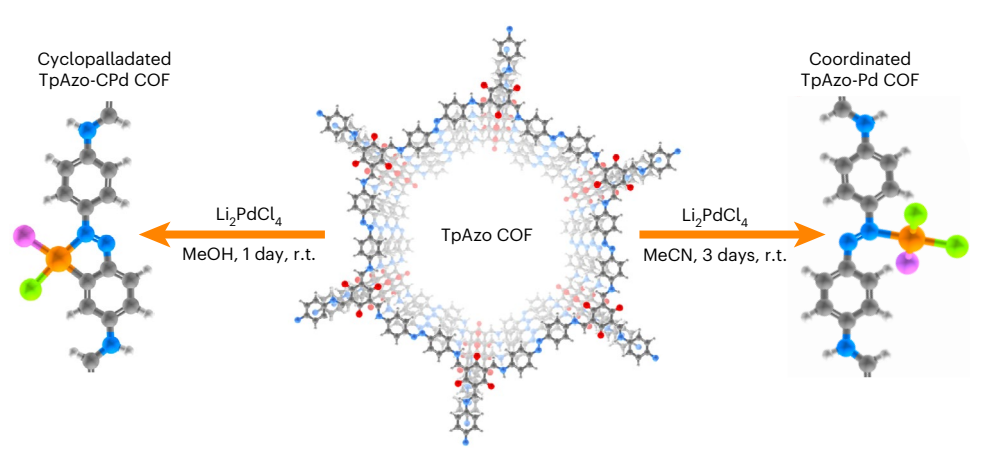


Fig. 1| **Schematic representation of TpAzo COF palladation.** Left: TpAzo-CPd COF obtained using methanol. Right: TpAzo-Pd COF obtained using acetonitrile. Grey, carbon; white, hydrogen; red, oxygen; blue, nitrogen; orange, palladium; green, chlorine; and purple, the representation of exchangeable ligands. r.t., room temperature.

One challenge in extending the light responsivity of COF photocatalysts into the NIR region is the relatively low energy of NIR light, which provides limited driving force for photocatalytic reactions. Under these circumstances, it is crucial for NIR COF photocatalysts to possess mitigated charge recombination, enabling efficient use of the absorbed NIR photon energy to drive the chemical conversion reactions. Although some strategies—such as linker protonation 14 , incorporation of linkers with extended π -conjugation 15 , or donoracceptor constructs 16 —have been developed to extend COF light absorption, only a limited number of strategies have successfully extended the absorption into the NIR region 16,17 , which further complicates the search for suitable NIR COF photoabsorbers through material screening.

Over the past decade, post-synthetic modification of COFs has been established as an effective approach to enrich the diversity and functionality of COFs. Among the various post-synthetic modification strategies, the metallation of COFs has drawn increasing attention in the field of photocatalysis, as it can introduce active sites for targeted reactions¹⁸. In 1965, Cope et al. 19 synthesized a cyclopalladated complex derived from azobenzene (Azo), documenting a pronounced red-shift in the optical characteristics. Subsequent investigations further diversified the chemistry of azo-cyclopalladated compounds, resulting in a variety of derived structures²⁰. These cyclopalladated complexes have exhibited remarkable catalytic performance across a range of reactions including C-C cross-coupling, reduction of aromatic nitro compounds and C-H activation²¹. Nevertheless, despite the recognized utility of cyclopalladated complexes, to the best of our knowledge, their integration into COFs remains unexplored so far.

Here we successfully applied cyclopalladation to the TpAzo COF, which is based on 1,3,5-triformylphloroglucinol (Tp) and Azo as the linker, following optimization of reaction conditions. We found that the use of methanol as the reaction solvent yields a highly functionalized cyclopalladated TpAzo COF (Fig. 1). The resulting COF exhibits a uniform distribution of site-isolated palladium atoms without notable formation of palladium nanoparticles, providing an effective solution to circumvent the formation of palladium nanoparticles—a synthetic challenge that is generally encountered in the integration of palladium complexes into COFs $^{22-24}$. Cyclopalladation induces a broadening of the light absorption of the COF, shifting the absorption edge into the NIR region. Taking advantage of this NIR light-harvesting capability, we here introduce a light-harvesting COF photocatalyst for photocatalytic solar energy conversion, affording the production of H_2O_2 —a widely used and valuable industrial chemical.

Results and discussion

Cyclopalladation of TpAzo COF

In the cyclopalladation of an azobenzene derivative, the formation of the carbon-metal bond involves deprotonation of the phenyl ring, resulting in the generation of HCl as a by-product when using Li₂PdCl₄. As a number of COFs are sensitive to acidic conditions, β-ketoenamine was adopted as the COF linkage in this work and TpAzo COF was prepared via a solvothermal route. Pyrrolidine was used as the reaction catalyst to enhance the crystallinity of TpAzo (ref. 25). The cyclopalladation was performed using Li₂PdCl₄ as a palladium source, which was prepared in situ from LiCl and PdCl₂. Li₂PdCl₄ solution was slowly added dropwise to a TpAzo COF dispersion under constant stirring to prevent palladium nanoparticle formation. Two reaction solvents, MeOH and MeCN, were compared for the cyclopalladation reaction. We found that using MeOH results in the formation of site-isolated cyclo-Pd complexes, whereas MeCN only results in coordinated palladium atoms (see below for details). To simplify the discussion, the pristine TpAzo COF is denoted TpAzo, and the post-palladation COF using MeCN or MeOH as solvents are denoted TpAzo-Pd and TpAzo-CPd, respectively.

After conducting the post-synthetic palladation on the pristine TpAzo, the amount of anchored palladium was quantified using inductively coupled plasma optical emission spectroscopy (ICP-OES), giving a palladium content of 2.76 ± 0.05 wt% for TpAzo-Pd and 12.60 ± 0.05 wt% for TpAzo-CPd (Supplementary Table 1). TpAzo-CPd exhibits a palladium content four times higher than that of TpAzo-Pd, indicating that the coordination of palladium atoms to TpAzo COF probably varies depending on the solvent used. The crystallinity of the pristine and palladium-functionalized COFs were studied by powder X-ray diffraction (PXRD) analysis. All three materials—namely, TpAzo, TpAzo-Pd and TpAzo-CPd-exhibit five distinct diffraction peaks (Fig. 2a) at $2\theta = 3.6^{\circ}$, 6.3°, 7.3°, 9.6° and 31.1° (Co K α_1 radiation), corresponding to the 100, 110, 200, 210 and 001 reflections, respectively²⁶. This observation suggests that the COF structure is robust enough to retain the crystallinity under the acidic reaction conditions and during the incorporation of palladium ions into the framework. Interestingly, TpAzo-CPd does exhibit noticeable alterations in the relative intensity of the reflections at 6.3° and 7.3° 2θ , which will be discussed in more detail in the following section.

Next, the impact on COF porosity afforded by the incorporation of palladium into the framework was assessed by examining N_2 sorption isotherms (Fig. 2b). Both the pristine COF and the palladated COFs exhibit typical isotherms of mesoporous adsorbents, characterized by the distinct inflection in nitrogen uptake at low relative pressure (centred around $0.1 P/P_0$)²⁷. The N_2 sorption isotherm for TpAzo-Pd

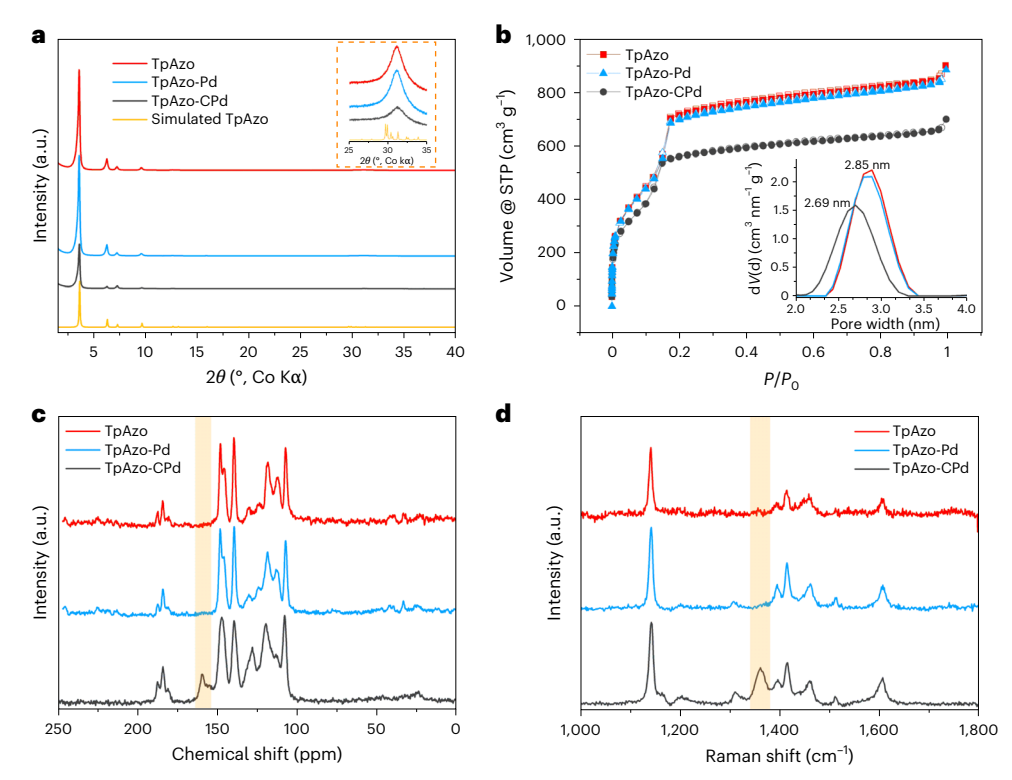


Fig. 2| **Structural characterization of TpAzo, TpAzo-Pd and TpAzo-CPd COFs. a**, Powder X-ray diffraction patterns, including a simulated TpAzo pattern. The inset graph shows a close-up of the region corresponding to the 001 reflection. **b**, N_2 sorption isotherms. Pore size distributions are displayed in the inset graph.

STP, standard temperature and pressure. \mathbf{c} , 13 C solid-state NMR. The shaded area highlights the C–Pd signal in TpAzo-CPd. \mathbf{d} , Raman spectra after baseline correction. The shaded area highlights the emerging vibrations in TpAzo-CPd.

closely resembles that of pristine TpAzo, whereas TpAzo-CPd exhibits a reduction in gas uptake, which is probably correlated with the substantial incorporation of the cyclo-Pd complex. TpAzo and TpAzo-Pd show very similar Brunauer–Emmett–Teller (BET) surface areas of 2,077 $\rm m^2\,g^{-1}$ and 2,064 $\rm m^2\,g^{-1}$, respectively, whereas the BET surface area of TpAzo-CPd decreases to 1,643 $\rm m^2\,g^{-1}$. Furthermore, TpAzo and TpAzo-Pd share the same pore size of 2.85 nm. In comparison, TpAzo-CPd shows a pore size of 2.69 nm—slightly smaller than TpAzo and TpAzo-Pd (Supplementary Figs. 8–10). The above results demonstrate that the limited palladium functionalization in TpAzo-Pd has a minor impact on the porosity of TpAzo COF. By contrast, the decreased pore size and BET surface area of TpAzo-CPd can be rationalized by the substantial incorporation of palladium species into the pore walls of the framework.

Next, solid-state nuclear magnetic resonance (ssNMR) and Raman spectroscopy were performed to confirm the success of cyclopalladation in TpAzo-CPd. As shown in Fig. 2c, the ¹³C-ssNMR spectra of all three samples exhibit distinct signals between 110 ppm and 140 ppm, and the signals at around 180 ppm assigned to the carbonyl carbon in the keto form of the Tp moiety are present all three samples. Although the majority of signals remained unchanged after cyclo-Pd complex incorporation, an additional peak centred at 159 ppm emerged for TpAzo-CPd. This can be attributed to the aromatic carbon directly bonded to palladium, as documented in the reported literature, which establishes the formation of an organometallic bond through cyclopalladation (see Supplementary Fig. 11 for a detailed assignment)^{28,29}. Furthermore, 2D heteronuclear correlation NMR (1H-13C HETCOR-NMR) was performed to investigate the proton-carbon correlation in TpAzo-CPd (Supplementary Fig. 12). The carbon signal at 159 ppm shows no coupling with any proton, which is consistent with the nature of a C-Pd bond. Moreover, Fig. 2c demonstrates that no obvious change in ¹³C signals is observed between TpAzo-Pd and TpAzo, even after extending the reaction time to ten days, indicating that no cyclopalladation takes place for TpAzo-Pd (Supplementary Fig. 13). Furthermore, ¹⁵N-ssNMR was performed on TpAzo COFs containing an ¹⁵N-enriched Azo linker (refer to the Supplementary Information for details). As displayed in Supplementary Fig. 12, TpAzo and TpAzo-Pd exhibit identical ¹⁵N-ssNMR spectra, implying a largely unchanged chemical environment of nitrogen atoms in TpAzo-Pd. In contrast, TpAzo-CPd shows a noticeable shift in its spectrum, with the signal for the NH linkage shifted from -243 to -239 ppm, and the signal for the azo nitrogen atoms shifted from -20 ppm to -31 ppm for pristine TpAzo COF and TpAzo-CPd, respectively (Supplementary Fig. 15). The success of cyclo-Pd complex formation in TpAzo-CPd was also confirmed by Raman and Fourier-transform infrared spectroscopy (FT-IR). As displayed in Fig. 2d and Supplementary Fig. 16, the appearance of the peak centred at 1,387 cm⁻¹ in the Raman spectrum and distinct changes in the fingerprint region of the FT-IR spectrum around 1,200 cm⁻¹ are observed for TpAzo-CPd, which can be assigned to the vibrational modes pertaining to the bonding between carbon and palladium atoms in the cyclo-Pd complex³⁰.

Putting the aforementioned structural characterization together, it can be inferred that C–Pd bonding is facilitated under conditions employing MeOH as the solvent, whereas the utilization of MeCN does not favour the formation of C–Pd bonding 31 . We rationalize the solvent effect by considering that MeOH (19.0 kcal mol 1) has a higher donor number than MeCN (14.1 kcal mol $^{-1}$) 32 , which may translate into a better proton accepting ability from azobenzene upon cyclopalladation (Supplementary Fig. 23).

Notably, the cyclopalladation of TpAzo COF enhances structural stability, as TpAzo-CPd maintains its crystallinity and integrity even after 24 h of immersion in 1 M KOH and 3 M HCl, superior to the TpAzo and TpAzo-Pd COFs (Supplementary Figs. 23–25).

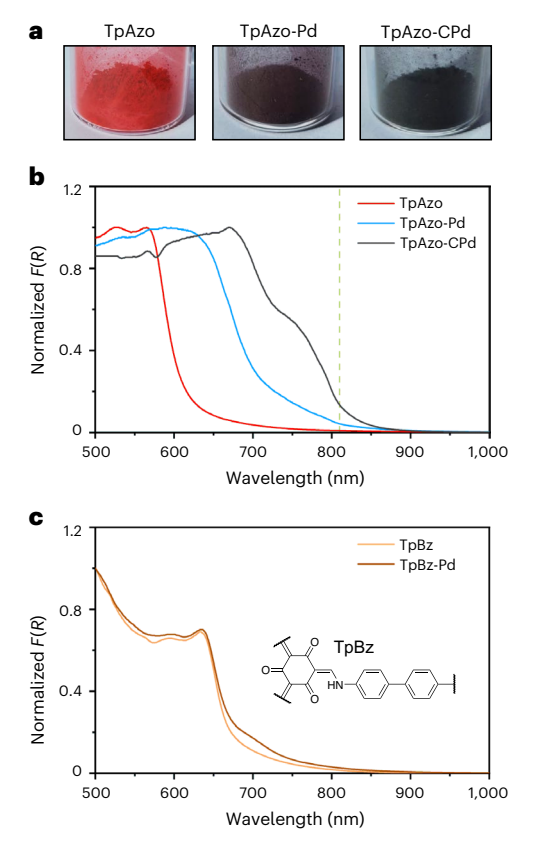


Fig. 3 | **Optical properties of palladated COFs. a**, Photographs of TpAzo, TpAzo-Pd and TpAzo-CPd COFs powders. **b,c**, Kubelka–Munk function (F(R)) from vis–NIR diffuse reflectance (R) spectra of TpAzo, TpAzo-Pd and TpAzo-CPd (**b**; the vertical dashed green line indicates 810 nm), and TpBz and TpBz-Pd (**c**; the inset represents the chemical structure of TpBz COF).

Optical properties

An obvious change in the colour of the COF powder is observed following the incorporation of palladium into TpAzo COF (Fig. 3a). Visible–NIR diffuse reflectance spectroscopy (vis–NIR DRS) was employed to investigate the effect of metal coordination on the optical properties of COFs. The pristine TpAzo COF shows strong visible light absorption with an onset at 599 nm (Supplementary Fig. 27), resulting in a reddish-coloured powder. When palladium was incorporated into the COF, a substantial broadening of the absorption range is obtained: the absorption onset of TpAzo is red-shifted to 692 nm for TpAzo-Pd and 804 nm for TpAzo-CPd (Fig. 3b, and Supplementary Figs. 28 and 29). These results indicate that the cyclopalladation in TpAzo COF enables the extension of light absorption into the NIR region. The influence of palladium on the optical properties of TpAzo COFs probably arises from a metal-to-ligand charge transfer transition, as commonly observed in cyclometallated complexes 33,34.

A series of control experiments were conducted to confirm whether the observed colour change was a result of palladium complexation. First, it has been demonstrated that the protonation of the COF linkage in acidic media can cause a substantial bathochromic shift in the absorption spectra 14 . To rule out this possibility, TpAzo COF was exposed to a methanolic solution of HCl at a concentration calculated to match the scenario in which all moles of PdCl $_2$ used in the palladation synthesis released an equivalent amount of protons in the form of HCl. This sample, referred to as TpAzo + HCl, exhibited an absorption spectrum almost identical to that of the pristine COF (Supplementary Fig. 33), thus disproving the notion that the broad light absorption of TpAzo-CPd is due to COF protonation.

Second, 4-dimethylaminoazobenzene, also known as methyl yellow (MY), was employed as a model molecule of TpAzo COF to evaluate the effect of cyclopalladation on optical properties, due to its structural similarity to the TpAzo fragment. Using the same palladation protocol, MY was successfully functionalized to MY-CPd (Supplementary Fig. 34). Notably, the light absorption spectra of these two samples exhibited a similar trend to that of TpAzo and TpAzo-CPd, where cyclopalladation extended the light absorption into the infrared region (with an approximately 100 nm shift in the absorption onset; Supplementary Fig. 35), confirming that the NIR light absorption of TpAzo-CPd originates from cyclo-Pd complexation.

Furthermore, a control COF containing benzidine rather than azobenzene (TpBz COF) was synthesized and used to understand the crucial role of azobenzene on the optical property change after palladium incorporation. As it has been reported that the ketoenamine linkage also coordinates with palladium ions²², using TpBz COF as a control system allows us to verify whether the observed red-shift in absorption is attributable to such coordination. Following the same synthetic protocol used for TpAzo-CPd, palladium was incorporated into TpBz COF (denoted TpBz-Pd). The palladium content of TpBz-Pd was determined to be 3.10 ± 0.03 wt% by ICP-OES, which is similar to that of TpAzo-Pd (2.76 ± 0.08 wt%); however, vis-NIR DRS spectra revealed that only a minor red-shift is obtained for TpBz-Pd compared with pristine TpBz COF, which contrasts the pronounced red-shift in TpAzo-Pd and TpAzo-CPd (Fig. 3c). This comparison suggests that the change in optical properties following palladium decoration is predominantly due to the coordination between palladium atom and azobenzene moiety, rather than the ketoenamine linkage. This result is consistent with the structural characterizations, which identify azobenzene as the primary site of palladium atom coordination.

Palladium environment in TpAzo-CPd COF

Having confirmed the presence of Pd–C bond formation and its optical properties, we next sought to more closely investigate the palladium coordination environment in TpAzo-CPd COF. First, to confirm the presence of chloride atoms in the COF structure, quantification of Cl was performed by elemental analysis (Supplementary Table 2), yielding a weight percentage of chloride of 6.22 wt%. Together with the palladium quantified by ICP-OES, the atomic ratio between palladium and chloride is estimated to be 1.42 (Supplementary Table 2). The atomic ratio of below 2 suggests the possible attachment of exchangeable ligands such as water or methanol to the complex^{28,31}. On this basis, we considered three different coordination scenarios to estimate the ratio of azo groups forming cyclopalladated complexes (Supplementary Fig. 38). The results indicate that approximately 60% of the azo groups in TpAzo-CPd are present as cyclopalladated complexes (Supplementary Fig. 38).

As the cyclopalladated azobenzene crystal structure (azobenzene-CPd) reveals that cyclopalladation can lead to a contraction of the azobenzene moiety (Supplementary Fig. 39), subtle structural modifications can be expected in TpAzo-CPd COF after cyclopalladation. As depicted in Fig. 4a–c and Supplementary Fig. 40, TpAzo-CPd shows a shift in the 100 (2θ of -0.017°) and 001 reflections (2θ of -0.128°) compared with TpAzo and TpAzo-Pd. This can be rationalized by the cyclopalladation resulting in a contraction of the Azo linker (Supplementary Fig. 39) as well as a slightly shortened π – π stacking distance due to the distortion of the cyclopalladation complex. In addition, Fig. 4b shows a relative intensity change of the 110 and 200 reflections after cyclopalladation. Such behaviour is due to the additional electron density to the COF pore in the form of -PdCl₂ (Supplementary Fig. 41).

Difference pair distribution function (dPDF) analysis was performed to further investigate the palladium coordination environment in TpAzo-CPd³⁵⁻³⁷. As shown in Fig. 4d, substantial peaks can be observed in the dPDF between TpAzo-CPd and TpAzo, particularly at

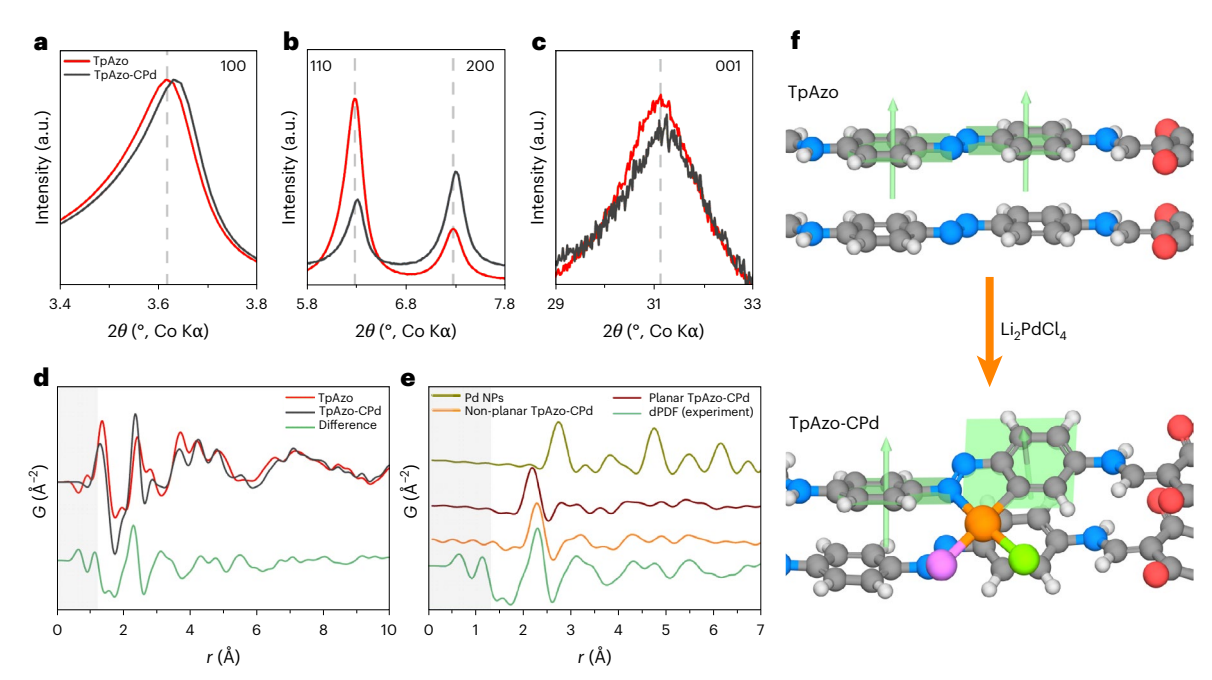


Fig. 4 | **Structural analysis of TpAzo-CPd.** a–c, Comparison of 100 (a), 110 and 200 (b) and 001(c) reflections of TpAzo and TpAzo-CPd PXRD patterns. d, Pair distribution function (G(r)) comparison of TpAzo-CPd and TpAzo, showing a modification in the local structure signal. The shaded grey area represents the low-r region most affected by systematic errors during the data processing.

 $\label{eq:comparison} \textbf{e}, Comparison of dPDF signals calculated from different models. NPs, nanoparticles. \textbf{f}, Scheme of proposed models of TpAzo and TpAzo-CPd. Grey, carbon; white, hydrogen; red, oxygen; blue, nitrogen; orange, palladium; green, chlorine; purple, exchangeable ligands; and light green, representation of the plane described by the phenyl ring and its perpendicular vector.$

r = 2.3 and 3.1, and between 4–6 Å, suggesting a coherent structure modification due to the presence of bound palladium complexes. Note that no major dPDF signals were obtained when comparing TpAzo-Pd and TpAzo (Supplementary Fig. 42), which further suggests a negligible structural change when using acetonitrile as the reaction solvent. Moreover, the absence of the peaks assigned to the metallic palladium structure (Fig. 4e) – specifically, the Pd–Pd distance at 2.7 Å–allows us to exclude the presence of palladium nanoparticles in TpAzo-CPd. As it has been reported that Pd(II) ions are easily transformed to palladium nanoparticles when synthesizing palladium-functionalized COFs²²⁻²⁴, dPDF suggests that our synthesis affords a large amount of Pd(II) complex incorporation without noticeable formation of palladium nanoparticles. Furthermore, the single-crystal structure of cyclopalladated azobenzene compounds reveals a distortion in planarity by the formation of the palladacycle, driven by the steric effect of the coordinated ligands and the adjacent protons³¹. We therefore also considered the possibility of a planarity change following the introduction of the palladium complex. Introducing a torsion angle of 30° between the two phenyl rings of the azobenzene (Fig. 4e) results in a better match of the nearest-neighbour palladium distance distribution, including Pd-C/N and Pd-Cl bond distances of ~2.0 Å and ~2.3 Å, respectively. Moreover, the non-planar model has a better fit in the 3-6 Å range than the planar one. Combining the above results and other simulations (Supplementary Fig. 43), it is inferred that a distortion of the TpAzo 2D framework is induced by the formation of the cyclopalladation complex (Fig. 4f).

Transmission electron microscopy (TEM), scanning electron microscopy (SEM) and X-ray photoelectron spectroscopy (XPS) were conducted to study the palladium site isolation and the palladium electronic environment in TpAzo-CPd. As shown in Fig. 5a, TpAzo-CPd displays crystalline domains with a lattice spacing of 2.67 nm (Supplementary Fig. 47). This spacing corresponds to the 100 reflection of TpAzo-CPd, and is well aligned with the distance obtained from the PXRD pattern. Furthermore, a negligible quantity of palladium nanoparticles was found as darker spots under transmission electron microscopy (TEM) (Supplementary Fig. 48). Energy-dispersive

X-ray spectroscopy coupled with scanning TEM (STEM-EDX) further suggests that palladium and chlorine are uniformly distributed and well-mixed with carbon in TpAzo-CPd, demonstrating homogeneous functionalization by cyclopalladation throughout the sample (Fig. 5b). Scanning electron microscopy images confirm the absence of palladium nanoparticles in TpAzo-CPd across micrometre-sized regions (Fig. 5c). The SEM images collected using an energy-selective backscattered electron detector (ESB) and a type II secondary electron detector (SE2) show no evidence of visible bright dots indicative of palladium nanoparticles. The effectiveness of SEM-ESB and SE2 characterization is validated by measuring a control sample, obtained by treating TpAzo-CPd with NaBH₄, thereby reducing the palladium complex to palladium nanoparticles (denoted TpAzo-CPd + NaBH₄). The SEM-ESB images of TpAzo-CPd + NaBH₄ reveal numerous bright dots signalling the presence of palladium nanoparticles. Further characterizations of TpAzo-CPd + NaBH₄ via FT-IR, Kubelka-Munk function analysis and XPS prove that the palladacycle is destroyed upon reduction (Supplementary Figs. 52-54). In the palladium 3d XPS spectrum of TpAzo-CPd, two distinct peaks appear at 337.9 eV and 343.2 eV, which correspond to the $3d_{5/2}$ and $3d_{3/2}$ core levels of Pd(II) ions forming a chlorinated palladium complex (Fig. 5d)^{38,39}. Furthermore, the peaks at 198.4 eV and 200.0 eV are observed in the Cl 3p XPS spectrum, and are attributed to the $2p_{3/2}$ and $2p_{1/2}$ core levels of a chloride species (Fig. 5d)⁴⁰. These results provide compelling evidence that the palladium in TpAzo-CPd mainly exists as isolated Pd(II) sites in the form of cyclopalladation complexes with chloride ions as the ligand.

Photocatalytic H₂O₂ production

The photocatalytic activity of TpAzo COFs under NIR light (810 nm LED) was evaluated through the generation of $\rm H_2O_2$ via the reduction of molecular oxygen in a $\rm 2e^-$ process (Fig. 6a). To investigate the thermodynamic ability of these COFs to reduce oxygen, the energy levels of the highest-occupied molecular orbital (HOMO) and the lowest-unoccupied molecular orbital (LUMO) were determined by electrochemical cyclic voltammetry (Supplementary Fig. 56–61).

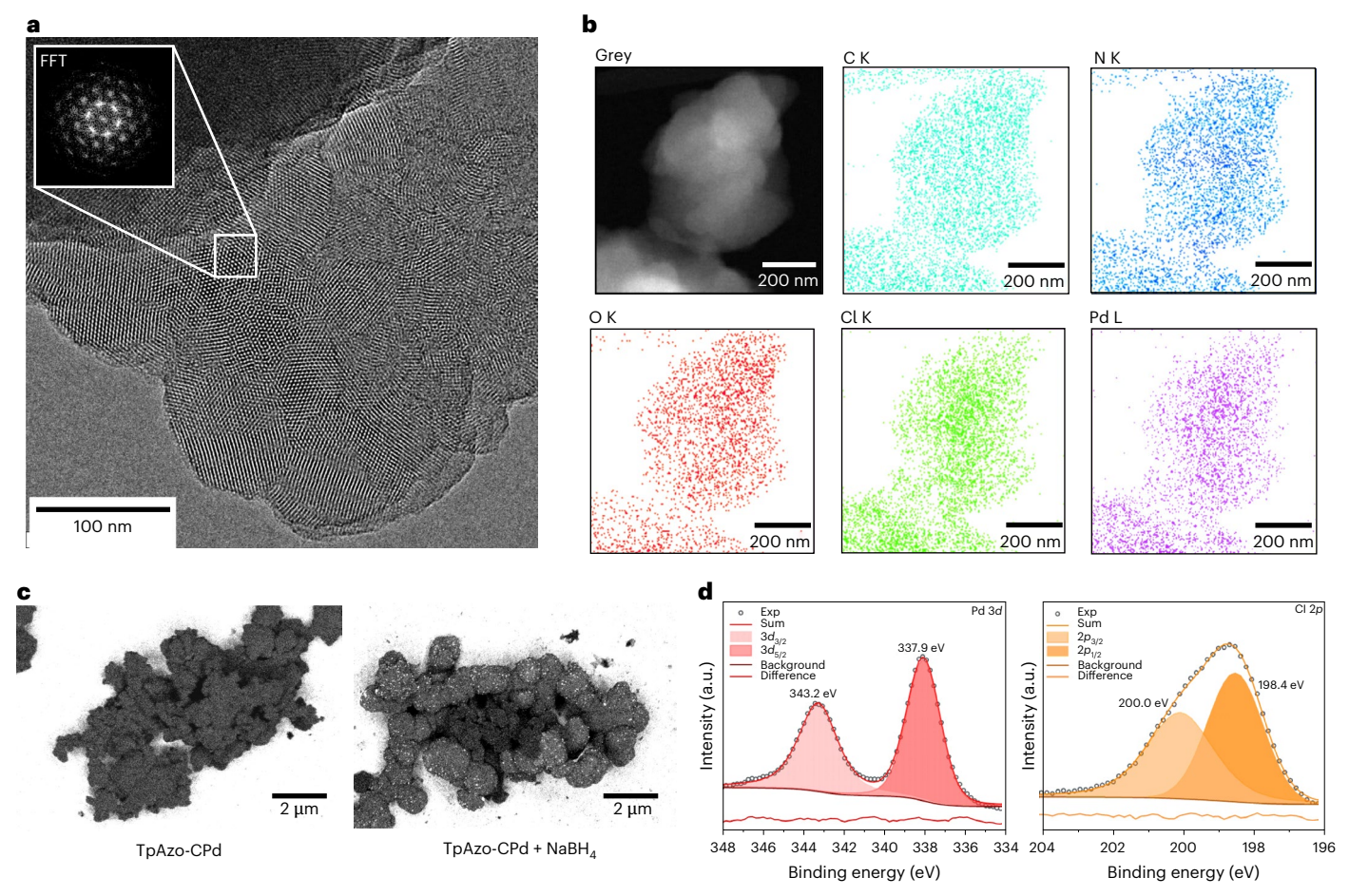
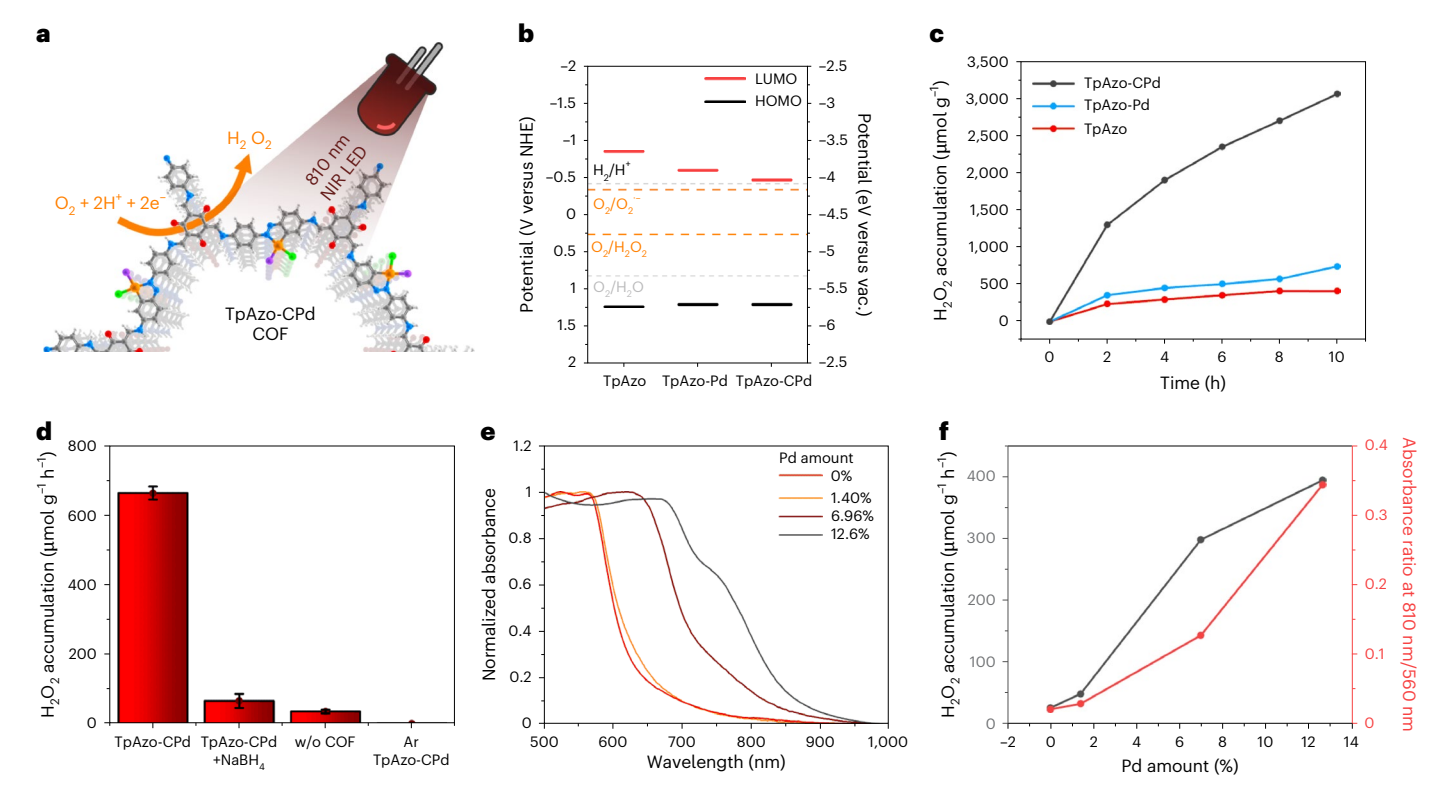


Fig. 5 | **Characterization of isolated palladium atoms in TpAzo-CPd COF. a**, High-resolution TEM image and fast Fourier transform of a selected area. **b**, STEM-EDX elemental mapping analysis of the area shown at the top left. **c**, SEM images using ESB/SE2 detectors. **d**, Palladium 3*d* and Cl 2*p* XPS spectra.

The three COFs show similar HOMO values (approximately 1.2 V versus NHE pH 7); however, different LUMO energy levels were obtained for TpAzo, TpAzo-Pd and TpAzo-CPd, which were located at $-0.9\,V$, $-0.6\,V$ and $-0.5\,V$, respectively, versus the NHE at pH 7 (Fig. 6b). We propose that LUMO energy level is altered by palladium coordination to the azo group. This probably perturbs the electronic structure of the N=N bond, which greatly contributes to the LUMO orbital due to its electron-accepting nature 41 . Nevertheless, the LUMO levels of all COFs thermodynamically satisfy the requirement of photocatalytic oxygen reduction via both a two-step superoxide radical pathway and via a one-step two-electron transfer process (Fig. 6b) 42 .

The photocatalytic production of H₂O₂ by TpAzo COFs was measured with an 810 nm LED using a constant oxygen flow of 100 ml min⁻¹, with benzyl alcohol used as the sacrificial electron donor, and the amount of photocatalyst optimized to 4 mg (Supplementary Fig. 64). As shown from the 10 h of continuous tests (Fig. 6c), TpAzo-CPd COF exhibited a higher H₂O₂ production rate (652.2 µmol g⁻¹ h⁻¹) than TpAzo-Pd COF (178.7 μmol g⁻¹ h⁻¹) and pristine TpAzo COF (119.5 µmol g⁻¹ h⁻¹) (all rates were calculated from the first 2 h of illumination). The cyclopalladated COF exhibited superior activity for H_2O_2 production under NIR irradiation when compared with different palladium coordination strategies or different COFs with similar palladium loading (Fig. 6a and Supplementary Fig. 65). To verify whether H_2O_2 is produced by photogenerated charges, we measured the H_2O_2 production rate for 4 h in the dark, which was followed by a period of illumination (Supplementary Fig. 66). Although 2.6 μmol of H₂O₂ was detected during the first hour for TpAzo-CPd under dark conditions, H_2O_2 production ceased thereafter. The H_2O_2 formed in the dark is probably attributable to the incipient self-oxidation of the TpAzo-CPd COF by the purged oxygen, since no H₂O₂ was detected under argon (Fig. 6d) and obtaining H₂O₂ via self-oxidation has been reported in other studies on molecular photocatalysts for H_2O_2 production⁴³. The FT-IR spectrum of TpAzo-CPd after a 10 h continuous illumination test remained identical with the pristine TpAzo-CPd (Supplementary Fig. 68). Apart from some photo-induced palladium reduction (up to 18%) after 10 hirradiation (Supplementary Fig. 69), no chemical structure changes were observed as a consequence of self-oxidation. After illumination, we observed 4 h of continuous H₂O₂ production at a rate of 551.9 µmol g⁻¹ h⁻¹, which is consistent with the H₂O₂ production rate in Fig. 6c, thus confirming that photogenerated charges of TpAzo-CPd COF were consumed to produce H_2O_2 . Excluding the small amounts of hydrogen peroxide produced in the dark, the apparent quantum yield of TpAzo-CPd at 810 nm was determined to be 2.2% when using BzOH as the sacrificial agent, and 0.4% when using MeOH (Supplementary

Several other control experiments were performed in an attempt to further understand the role of TpAzo-CPd COF for NIR photocatalytic H_2O_2 production. First, we verified that although palladium nanoparticles can integrate NIR light absorption with catalytic properties, the cyclopalladation complex exhibited superior performance in terms of NIR photocatalytic H_2O_2 production compared with palladium nanoparticles. As shown in Fig. 6d, only 65.8 μ mol g⁻¹h⁻¹of H_2O_2 was obtained with TpAzo-CPd + NaBH₄, wherein the cyclopalladation complex was disassembled into palladium nanoparticles, as demonstrated in Fig. 4c. Furthermore, reducing the palladium loading amount in TpAzo-CPd also led to decreased light absorption at 810 nm (Fig. 6e). At a palladium



 $\label{eq:Fig.6} Fig. 6 | Photocatalytic production of H_2O_2 under NIR light. a, Schematic representation of H_2O_2 production under 810 nm LED. Grey, carbon; white, hydrogen; red, oxygen; blue, nitrogen; orange, palladium; green, chlorine; purple, exchangeable ligands. b, Energy levels of the COFs versus vacuum (vac.) and versus normal hydrogen electrode (NHE). Reference water splitting potentials (light grey) are defined at pH 7. c, Photocatalytic production of H_2O_2 and H_2O_2 are defined at pH 7. c.$

under 810 nm LED irradiation. ${f d}$, Control experiments on ${\bf H}_2{\bf O}_2$ production after 2 h of illumination. Error bars were calculated from three independent photocatalytic experiments. Data are presented as mean value \pm s.e.m. ${\bf e}$, Vis–NIR absorbance spectra from diffuse reflectance spectroscopy of TpAzo-CPd COF with different palladium amounts. ${\bf f}$, ${\bf H}_2{\bf O}_2$ production from a series of TpAzo-CPd COFs with different palladium amount and their relative absorbance at 810 nm.

loading of 1.4 wt%, the light absorption at 810 nm was nearly identical to that of TpAzo, and the $\rm H_2O_2$ production rate of this sample under 810 nm illumination became negligible (Fig. 6f and Supplementary Fig. 71). These findings underscore the critical role of extended light absorption on photocatalytic $\rm H_2O_2$ production as cyclopalladation of the COF proceeds (Fig. 6f).

A series of control experiments and quantum-chemical calculations were performed to better understand the H₂O₂ production mechanism.. First, several scavengers were used to elucidate the intermediates involved in the photocatalytic reaction (see Supplementary Information for more details); among them, p-benzoquinone (a known O₂-/OOH radical scavenger) considerably reduced H₂O₂ generation (Supplementary Fig. 75b). This suggests the critical role of O₂⁻⁻/OOH radicals during hydrogen peroxide production, which is typical of the stepwise 1e⁻ pathway in the 2e⁻ oxygen reduction reaction^{3,44}. Furthermore, density functional theory calculations were performed. The resulting energy profiles for the proposed reaction mechanisms agree with the above argument, showing that the stepwise 1e⁻ pathway has lower energies than the direct 2e⁻ pathway (Supplementary Figs. 79 and 82). Moreover, it was observed that participation of the palladium atom in TpAzo-CPd results in lower energies than those involving the hydrogen atom of pore-oriented TpAzo, which corroborates the active role of the palladium centre in the stepwise 1e oxygen reduction (Supplementary Figs. 78 and 79).

Conclusion

In summary, we have developed a post-synthetic functionalization scheme, incorporating a palladacycle into the azobenzene COF backbone by a quantitative cyclopalladation reaction. The resulting COF, TpAzo-CPd, extends light absorption into the NIR spectrum region

and enables the demonstration of a COF NIR photocatalyst. Structural characterizations, including solid-state NMR and Raman spectroscopy, establish that the cyclopalladation complex is obtained using methanol as the reaction solvent, whereas acetonitrile only facilitates non-specific N-Pd coordination without the formation of a C-Pd bond. The cyclopalladated COF (TpAzo-CPd) retains the crystallinity of TpAzo and exhibits a uniform distribution of palladacycles in the frameworks without noticeable formation of palladium nanoparticles. Under 810 nm LED illumination, TpAzo-CPd can produce H₂O₂ via photocatalytic oxygen reduction. Further investigations confirm that the NIR light absorption induced by cyclopalladation contributes photogenerated charges crucial for photocatalytic H₂O₂ production. Therefore, this work not only expands the scope of post-synthetic functionalization of COFs by introducing cyclopalladation to the toolbox, but also demonstrates the potential of COFs in NIR photocatalysis. We anticipate that our results will stimulate the rational design of NIR-responsive COFs and advance their applications in harvesting NIR light for solar fuel generation, chemical synthesis, and biomedical applications-particularly in photodynamic therapy for cancer treatment, where NIR light offers considerable advantages.

Methods

Synthesis of COFs

To synthesize TpAzo and TpBz COFs, a pyrrolidine-catalysed procedure was employed to attain highly crystalline TpAzo COF. In a typical COF synthesis, 0.47 mmol of the respective amine (101.3 mg of Azo and 86.2 mg of Bz) and 0.34 mmol of Tp (71.3 mg) were combined within a 6 ml Biotage high-precision glass vial. Subsequently, 4 ml of anhydrous 1,4-dioxane and 80 μ l of pyrrolidine (used as a catalyst) were added to the vial. The vial was sealed with a septum cap and subjected to 10 min

of sonication to achieve a homogenous dispersion. The reaction was kept at 120 °C on a hot plate without stirring for three days. Upon completion of the reaction period, the vial was allowed to cool naturally to room temperature and then unsealed. The resulting COF powder was filtered and rinsed with THF. To eliminate any residual linkers and catalyst, the COF powder was subjected to 24 h of Soxhlet extraction. Finally, the solvent was exchanged with methanol, and the powder was dried using supercritical CO $_2$.

Palladation of COFs

Consistent reaction conditions were maintained across the solvents to investigate their influence over the palladation process. Initially, Li₂PdCl₄ was prepared by vigorously stirring 5 mg of PdCl₂ and 2.5 mg of LiCl in 10 ml of the respective solvent (MeOH or MeCN) for a duration of 3 h. In a separate 20 ml glass vial, 10 mg of COF was dispersed in 5 ml of the solvent using sonication for 10 min. The COF dispersion was then stirred while the previously prepared palladium solution was added dropwise over approximately 10 min at room temperature. The reaction time was set at 24 h for MeOH and extended to 72 h for MeCN. Upon completion of the reaction time, the resulting powder was filtered and thoroughly washed with a substantial volume of the corresponding solvent (MeOH or MeCN, as appropriate to each case). Finally, the palladated COF powder was air-dried overnight.

To synthesize TpAzo-CPd COFs with different palladium content, the procedure described above was followed but the amount of Li_2PdCl_4 methanolic solution (0.5 mg of PdCl $_2$ ml $^{-1}$) was modified accordingly: 10 ml for 12.6 wt%, 7 ml for 9.02 wt%, 5 ml for 6.96 wt%, 2.5 ml for 4.88 wt%, 1 ml for 3.02 wt% and 0.5 ml for 1.40 wt% of Pd.

Synthesis of TpAzo-CPd + NaBH₄

To reduce the palladium ions present in the cyclopalladated COF, 20 mg of as synthesized TpAzo-CPd COF was dispersed in 5 ml of MeOH. Then, under continuous stirring, 10 ml of 0.3 M methanolic NaBH $_{\rm 4}$ solution was added dropwise at room temperature. After 24 h of reaction, the COF was filtered and washed with copious amount of methanol. A dark red powder was obtained by air drying the sample overnight.

H₂O₂ quantification

The quantification of H_2O_2 was conducted through a spectrophotometric method based on the triiodide procedure. Specifically, 0.5 ml of filtered reaction solution (passed through by a 0.22 μ m hydrophilic polytetrafluoroethylene filter) was mixed with 1 ml of 0.1 M aqueous potassium iodide solution and 1 ml of aqueous 0.4 M potassium hydrogen phthalate solution. The resulting mixture was shielded from light for 30 min before UV–visible absorption measurement. To establish a calibration curve, fresh solutions of potassium iodide and potassium hydrogen phthalate were prepared weekly, and the curve points were generated using a commercial 30 wt% H_2O_2 solution and Milli-Q water.

Photocatalytic H₂O₂ production

In a typical photocatalytic experiment, 4 mg of COF was sonicated in 9 ml of Milli-Q water for 10 min. Next, 1 ml of sacrificial agent (usually benzyl alcohol) was added to the dispersion. The dispersion was then incorporated into a glass reactor with a quartz top window. The COF dispersion was stirred (200 r.p.m.) and purged with oxygen gas (100 ml min $^{-1}$) for 10 min before illumination. Finally, the reaction was continuously purged and stirred for 2 h under top illumination using a ThorLabs 810 nm mounted LED (M810L5) at full power. A xenon lamp (Newport, 300 W) equipped with a water filter, a dichroic mirror, and a 420 nm cutoff filter were used for solar simulator experiments. For H_2O_2 production longer than 2 h (Fig. 6c), stirring and illumination were stopped at specific intervals, and the dispersion was allowed to settle undisturbed for 2 min to separate the aqueous phase (top) from the benzyl alcohol phase (bottom). Next, 0.7 ml of the aqueous phase containing H_2O_2 was withdrawn using a syringe and

polytetrafluoroethylene filter. Subsequently, 0.7 ml of Milli-Q water was added back to the reaction mixture to maintain a constant reaction volume. Before resuming illumination, the reactor was purged with $\rm O_2$ gas for 10 min to restore the oxygen atmosphere. Note that additional methods can be found in the Supplementary Information.

Data availability

All data that support the findings of this study are available in the Supplementary Information. A dataset has been created with source data, at https://doi.org/10.18419/darus-4626 (ref. 45).

References

- Côté Adrien, P. et al. Porous, crystalline, covalent organic frameworks. Science 310, 1166–1170 (2005).
- 2. Lyu, H., Li, H., Hanikel, N., Wang, K. & Yaghi, O. M. Covalent organic frameworks for carbon dioxide capture from air. *J. Am. Chem.* Soc. **144**, 12989–12995 (2022).
- Liao, Q. et al. Regulating relative nitrogen locations of diazine functionalized covalent organic frameworks for overall H₂O₂ photosynthesis. Angew. Chem. Int. Ed. 62, e202310556 (2023).
- Xue, R., Liu, Y.-S., Huang, S.-L. & Yang, G.-Y. Recent progress of covalent organic frameworks applied in electrochemical sensors. ACS Sens. 8, 2124–2148 (2023).
- Grunenberg, L. et al. Postsynthetic transformation of imine- into nitrone-linked covalent organic frameworks for atmospheric water harvesting at decreased humidity. J. Am. Chem. Soc. 145, 13241–13248 (2023).
- Nguyen, H. L. Covalent organic frameworks for atmospheric water harvesting. Adv. Mater. 35, 2300018 (2023).
- Sridhar, V. et al. Designing covalent organic framework-based light-driven microswimmers toward therapeutic applications. Adv. Mater. 35, 2301126 (2023).
- 8. Ghosh, P. & Banerjee, P. Drug delivery using biocompatible covalent organic frameworks (COFs) towards a therapeutic approach. *Chem. Commun.* **59**, 12527–12547 (2023).
- Stegbauer, L., Schwinghammer, K. & Lotsch, B. V. A hydrazone-based covalent organic framework for photocatalytic hydrogen production. *Chem. Sci.* 5, 2789–2793 (2014).
- Rath B. B., Krause S. & Lotsch B. V. Active site engineering in reticular covalent organic frameworks for photocatalytic CO₂ reduction. Adv. Funct. Mater. 34, 2309060 (2023).
- Lin, G. et al. 3D porphyrin-based covalent organic frameworks. J. Am. Chem. Soc. 139, 8705–8709 (2017).
- Xiao, G. et al. Application of electron-rich covalent organic frameworks COF-JLU25 for photocatalytic aerobic oxidative hydroxylation of arylboronic acids to phenols. *Eur. J. Org. Chem.* 2021, 3986–3991 (2021).
- Li, B. et al. Photocatalysis driven by near-infrared light: materials design and engineering for environmentally friendly photoreactions. ACS ES&T Eng. 1, 947–964 (2021).
- Yang, J. et al. Protonated imine-linked covalent organic frameworks for photocatalytic hydrogen evolution. *Angew. Chem. Int. Ed.* 60, 19797–19803 (2021).
- Wang, X. et al. Sulfone-containing covalent organic frameworks for photocatalytic hydrogen evolution from water. *Nat. Chem.* 10, 1180–1189 (2018).
- Xia, Y., Zhang, W., Yang, S., Wang, L. & Yu, G. Research progress in donor–acceptor type covalent organic frameworks. *Adv. Mater.* 35, 2301190 (2023).
- 17. Bessinger, D., Ascherl, L., Auras, F. & Bein, T. Spectrally switchable photodetection with near-infrared-absorbing covalent organic frameworks. *J. Am. Chem.* Soc. **139**, 12035–12042 (2017).
- Segura, J. L., Royuela, S. & Mar Ramos, M. Post-synthetic modification of covalent organic frameworks. *Chem. Soc. Rev.* 48, 3903–3945 (2019).

- Cope, A. C. & Siekman, R. W. Formation of covalent bonds from platinum or palladium to carbon by direct substitution. *J. Am. Chem. Soc.* 87, 3272–3273 (1965).
- Nguyen, T. H. L., Gigant, N. & Joseph, D. Advances in direct metal-catalyzed functionalization of azobenzenes. ACS Catal. 8, 1546–1579 (2018).
- Dupont, J., Consorti, C. S. & Spencer, J. The potential of palladacycles: more than just precatalysts. *Chem. Rev.* 105, 2527–2572 (2005).
- Ding, S.-Y. et al. Construction of covalent organic framework for catalysis: Pd/COF-LZU1 in Suzuki–Miyaura coupling reaction. J. Am. Chem. Soc. 133, 19816–19822 (2011).
- Lin, S. et al. A triazine-based covalent organic framework/ palladium hybrid for one-pot silicon-based cross-coupling of silanes and aryl iodides. RSC Adv. 5, 41017–41024 (2015).
- Liu, J. et al. Palladium nanoparticles on covalent organic framework supports as catalysts for Suzuki-Miyaura cross-coupling reactions. ACS Appl. Nano Mater. 4, 6239–6249 (2021).
- Wang, R., Kong, W., Zhou, T., Wang, C. & Guo, J. Organobase modulated synthesis of high-quality β-ketoenamine-linked covalent organic frameworks. *Chem. Commun.* 57, 331–334 (2021).
- Chandra, S. et al. Phosphoric acid loaded azo (-N=N-) based covalent organic framework for proton conduction. *J. Am. Chem.* Soc. **136**, 6570–6573 (2014).
- Sing, K. S. W. Reporting physisorption data for gas/solid systems with special reference to the determination of surface area and porosity (Recommendations 1984). *Pure Appl. Chem.* 57, 603–619 (1985).
- Ćurić, M., Babić, D., Višnjevac, A. & Molčanov, K. Simple route to the doubly ortho-palladated azobenzenes: building blocks for organometallic polymers and metallomesogens. *Inorg. Chem.* 44, 5975–5977 (2005).
- Nikolaeva, M. V., Bogdanova, E. K. & Puzyk, M. V. Azobenzene palladium(II) complexes with β-diketones. Russ. J. Gen. Chem. 87, 485–488 (2017).
- Bjelopetrović, A. et al. Mechanism of mechanochemical C-H bond activation in an azobenzene substrate by Pd^{II} catalysts. Chem. Eur. J. 24, 10672–10682 (2018).
- Bjelopetrović, A. et al. A detailed kinetico-mechanistic investigation on the palladium C-H bond activation in azobenzenes and their monopalladated derivatives. *Inorg. Chem.* 59, 17123–17133 (2020).
- 32. Gutmann V. in Coordination Chemistry in Non-Aqueous Solutions (ed. Gutmann, V.) 12–34 (Springer, 1968).
- 33. Chakraborty, I., Carrington, S. J. & Mascharak, P. K. Design strategies to improve the sensitivity of photoactive metal carbonyl complexes (photoCORMs) to visible light and their potential as CO-donors to biological targets. Acc. Chem. Res. 47, 2603–2611 (2014).
- Maestri, M., Balzani, V., Deuschel-Cornioley, C. & Zelewsky A. V. in Advances in Photochemistry (eds Volman, D. H. et al.) 1–68 (Wiley, 1992)
- 35. Terban, M. W. et al. Atomic resolution tracking of nerve-agent simulant decomposition and host metal-organic framework response in real space. *Commun. Chem.* **4**, 2 (2021).
- Copeman, C. et al. Adsorptive removal of iodate oxyanions from water using a Zr-based metal-organic framework. Chem. Commun. 59, 3071–3074 (2023).
- Terban, M. W. & Billinge, S. J. L. Structural analysis of molecular materials using the pair distribution function. *Chem. Rev.* 122, 1208–1272 (2022).
- Chu, C. et al. Neighboring palladium single atoms surpass isolated single atoms for selective hydrodehalogenation catalysis. Nat. Commun. 12, 5179 (2021).

- Muravev, V. et al. Interface dynamics of Pd–CeO₂ single-atom catalysts during CO oxidation. Nat. Catal. 4, 469–478 (2021).
- 40. Militello, M. C. & Simko, S. J. Palladium chloride (PdCl₂) by XPS. Surf. Sci. Spectra **3**, 402–409 (1994).
- Wu, H. et al. The linkage-moderated covalent organic frameworks with —C=N— and —N=N— on charge transfer kinetics towards the robust photocatalytic hydrogen activity. Small 19, 2304367 (2023).
- 42. Freese, T., Meijer, J. T., Feringa, B. L. & Beil, S. B. An organic perspective on photocatalytic production of hydrogen peroxide. *Nat. Catal.* **6**, 553–558 (2023).
- 43. Yang, H. et al. Packing-induced selectivity switching in molecular nanoparticle photocatalysts for hydrogen and hydrogen peroxide production. *Nat. Nanotechnol.* **18**, 307–315 (2023).
- Zhao, W. et al. Accelerated synthesis and discovery of covalent organic framework photocatalysts for hydrogen peroxide production. J. Am. Chem. Soc. 144, 9902–9909 (2022).
- Andrés, R.-C. Cyclopalladation of a Covalent Organic Framework for Near-Infrared Light-Driven Photocatalytic Hydrogen Peroxide Production (DaRUS, 2024); https://doi.org/10.18419/darus-4626

Acknowledgements

We gratefully acknowledge financial support from the Deutsche Forschungsgemeinschaft (DFG, German Research Foundation) under grant no. TRR 247-388390466 (project A09, S project); grant no. 358283783—SFB 1333/2 2022 (project AO3); grant no. 444632635— CRC325 (project C5); the DFG Cluster of Excellence e-conversion—EXC 2089/1-390776260; the Max Planck Society, Max Planck Fellowship programme; the Center for NanoScience; and the Bavarian Research Network SolTech. We thank A. Schulz (FKF-MPI) for performing the Raman measurements, N. Weiß for conducting the thermogravimetric analysis, and V. Srot and K. Hahn (MPI-FKF) for the STEM experiments. We acknowledge DESY (beamline PO2.1, Hamburg, Germany)—a member of the Helmholtz Association HGF—for providing access to experimental facilities. N.G. thanks the Spanish Ministry of Science & Innovation for the 'Ramon y Cajal' Program (RYC2018-023888-I) and the support via the grant PID2021-128805NA-I00 funded by MCIN/AEI/10.13039/501100011033 and by the European Union Next Generation EU/PRTR. This project has also received funding from the European Research Council (ERC) under the European Union's Horizon 2020 research and innovation programme (grant no. 948829).

Author contributions

A.R.C. and L.Y. led the project. A.R.C. performed the syntheses and experiments. M.W.T. analysed the PDF data and performed PDF simulation. M.P. contributed to syntheses and material characterization. E.A.R. and N.G. conducted spectroscopic experiments and analysed the data. D.G. performed quantum-chemical calculations. R.H. performed XPS measurements. V.D. performed TEM experiments and supported in structure analysis. I.M. conducted ssNMR and assisted in its interpretation. M.E. performed PDF experiments at the synchrotron and supported data interpretation. C.O., N.G., R.E.D., L.Y. and B.V.L. conceived and supervised the research, discussed the data, and co-authored the paper. All authors reviewed and commented on the paper.

Funding

Open access funding provided by Max Planck Society.

Competing interests

The authors declare no competing interests.

Additional information

Supplementary information The online version contains supplementary material available at https://doi.org/10.1038/s44160-024-00731-1.

Correspondence and requests for materials should be addressed to Liang Yao or Bettina V. Lotsch.

Peer review information *Nature Synthesis* thanks Huijun Li and Liping Wang for their contribution to the peer review of this work. Primary Handling Editor: Alexandra Groves, in collaboration with the *Nature Synthesis* team.

Reprints and permissions information is available at www.nature.com/reprints.

Publisher's note Springer Nature remains neutral with regard to jurisdictional claims in published maps and institutional affiliations.

Open Access This article is licensed under a Creative Commons Attribution 4.0 International License, which permits use, sharing, adaptation, distribution and reproduction in any medium or format, as long as you give appropriate credit to the original author(s) and the source, provide a link to the Creative Commons licence, and indicate if changes were made. The images or other third party material in this article are included in the article's Creative Commons licence, unless indicated otherwise in a credit line to the material. If material is not included in the article's Creative Commons licence and your intended use is not permitted by statutory regulation or exceeds the permitted use, you will need to obtain permission directly from the copyright holder. To view a copy of this licence, visit http://creativecommons.org/licenses/by/4.0/.

© The Author(s) 2025